Article

The Effect of Fe on the Mechanical Properties of Stellite 6

Min Ah Baek [1,2], Gyu Byeong Kang [1], Gyeong Chan Suk [1], Seong Chan Hong [1], Young Do Kim [2,*] and Tae-Wook Na [1,*]

1   Functional Materials and Components R&D Group, Korea Institute of Industrial Technology, Gangneung 25440, Republic of Korea; alsa154@kitech.re.kr (M.A.B.)
2   Division of Materials Science and Engineering, Hanyang University, Seoul 133791, Republic of Korea
*   Correspondence: ydkim1@hanyang.ac.kr (Y.D.K.); arkasa86@kitech.re.kr (T.-W.N.)

Abstract: Stellite 6 is a Co-based alloy with excellent wear and corrosion resistance, resulting in it frequently being used as a hard-facing material. The main defect that occurs in the hard-facing process is the peeling of the hard-facing layer, which is caused by thermal stress due to differences in thermal expansion coefficients. This peeling phenomenon can be prevented by using a material with an intermediate coefficient of thermal expansion as a buffer layer. Component surfaces are strengthened through a technique called hard-facing, which increases the components' resistance to wear. In order to increase the wear and corrosion resistance of metal components, a high-hardness substance is usually coated onto their surface. Grinding is carried out to smooth the surface after the material is welded onto the base component. Small pieces, also referred to as "scrap", are frequently produced during this surface machining procedure. In the hard-facing process, scrap containing a mixture of base material and Stellite 6 is generated during material processing. If this scrap can be used as a buffer layer, the cost of raw materials can be reduced through the recycling of resources, and the overall energy consumption for recycling can be reduced because the process of separating Stellite 6 from the scrap is eliminated. In this study, the physical properties of Stellite 6 with Fe added were explored to determine whether the scrap produced could be used as a buffer layer. When iron was added to the mixture, the amount of carbide decreased, in addition to the wear resistance and hardness decreasing. Regarding the thermal expansion coefficient, the thermal expansion coefficient of Stellite 6 was found to be 15.879 μm/m·°C at 300 °C, and that of Stellite 6 with 40% Fe added was found to be 14.313 μm /m·°C at 300 °C. The thermal expansion coefficient of carbon steel is reported to be 12.8 μm /m·°C at 300 °C; thus, Stellite 6 with 40% Fe can be used as a buffer layer for Stellite 6 and carbon steel because of its suitable thermal expansion coefficient.

Keywords: Stellite 6; hard-facing; buffer layer

1. Introduction

Stellite 6 is a Co-based alloy containing Cr, W, and C and has excellent high-temperature strength, wear resistance, and corrosion resistance. These alloys are widely utilized in numerous industries, such as oil and gas, machinery, wood, cutting, automotive, paper, and food processing. Chromium, being the major alloying element of Stellite 6, provides better corrosion resistance properties, and the formation of carbides contributes to increasing strength. In addition, it also acts as a strengthening element through the formation of a solid solution. The presences of tungsten (W) and molybdenum (Mo) provide high strength through precipitation hardening, resulting in the formation of (Mo and W) carbides possessing adequate ductility and high density [1]. In particular, Stellite 6 has excellent wear and corrosion resistance due to its physical and chemical properties and is used as a hard-facing material for various materials [2–5].

One of the defects that occurs in the hard-facing process is delamination. This means that the base material and the hardened layer separate and fall away [6]. The primary cause of the surface peeling phenomenon is variations in the coefficient of thermal expansion. The

surface peeling phenomenon involves the separation of the coated area that has been hard-faced to prevent wear and corrosion. This indicates that the corrosion-resistant layer has been removed, which means that new hard-facing will need to be applied. Should this issue continue, it may result in both resource waste and inefficiencies in the processes involved. Creating a buffer layer is one technique to stop this from happening. The buffer layer is mainly made of a material with a thermal expansion coefficient intermediate between the base material and the hardened layer material [3].

For face-hardened steel using Stellite 6, Inconel is used as a buffer layer material to prevent delamination [7]. In general, after hard-facing processing using Stellite 6, a process to size the product is essential, and at this time, scrap mixed with Stellite 6 and the base material is generated. If these scraps are used as buffer layer materials, the cost of purchasing such materials can be reduced through resource recycling, and the total energy consumed in the process can also be reduced.

In order to use the produced scrap as a buffer layer, it is necessary to understand how the physical properties change when mixing the base material Fe and Stellite 6. In particular, it is imperative to confirm the coefficient of thermal expansion. The buffer layer should be checked to ensure that it can accommodate the deformation.

The problem and possibility of recycling scrap produced after hard-facing with Stellite were not well explained in earlier studies. Therefore, the purpose of this study is to explore the possibility of recycling such waste material. In particular, we seek to determine if resource recycling is practical in cases where the scrap contains a given quantity of base material and to examine its properties. In this study, when Fe was mixed and dissolved in Stellite 6, the physical properties of Stellite 6 were evaluated according to the concentration of Fe, and whether it could be used as a buffer layer material was also evaluated.

2. Materials and Methods

Selecting the appropriate buffer layer requires consideration of the thermal expansion coefficient. We anticipated that the base material and buffer layer's thermal expansion coefficients would coincide if their ratios were similar. However, because of the significant difference between the thermal expansion coefficients of Fe and Stellite, we concluded that a greater than 50% increase in the fraction of Fe in the base material was necessary to equal Fe's coefficient. Studies were therefore conducted with Fe added at 20% intervals. Fe concentrations of 20 weight percent (Sample A), 40 weight percent (Sample B), and 60 weight percent (Sample C) were created in order to examine the effects of Fe on the physical properties of Stellite 6 to ensure that the sample ingots were ready. To prepare ingots of samples, Stellite 6 with the chemical composition shown in Table 1 and pure Fe (99.99%) were used. The Stellite welding rods used in this experiment were sourced from UTP Schweiss Material (Bremerhaven, Germany). These welding rods were manufactured by the aforementioned company and are presumed to have been produced through a continuous casting process. Ingots of samples were manufactured via vacuum induction melting (VIM). The samples were preheated with the power of 4 kw for 5 min, and then, the power was set to 14 kw and maintained until the temperature reached 1400 °C before we increased the power to 16 kw. The average dissolution time was about 20 min, and the maximum temperature was 1600 °C. The samples were melted in an argon atmosphere of 10^{-4} torr, with an alumina crucible of 105 mm in diameter and 180 mm in height. We used a graphite mold with a volume of 483.84 cm^3 and a size of 54 mm in width, 56 mm in length, and 160 mm in height. The size of the sample ingot was 50 mm in width, 50 mm in length, and 50 mm in height. Using the samples produced in this way, specimens were prepared for SEM observation, XRD analysis, wear tests, and compression tests. The ingredients of the ingots were confirmed through inductively coupled plasma spectrometry (ICP) analysis, with the results shown in Table 2.

Table 1. Chemical composition of Stellite 6.

Sample Name	Element and Content (wt%)			
	Co	Cr	W	C
Stellite 6	66.95	27.12	4.63	1.29

Table 2. Chemical compositions of samples observed by ICP.

Sample Name	Element and Content (wt%)				
	Co	Cr	W	C	Fe
Stellite 6	63.68	27.42	6.65	1.43	0.82
Sample A	52.03	20.81	5.43	1.02	20.71
Sample B	38.47	16.16	3.23	0.78	41.36
Sample C	26.84	10.61	2.22	0.54	59.79

The microstructure of the alloys was observed using a scanning electron microscope (SEM) (Quanta FEG 250, FEI, Lausanne, Switzerland). For microstructure analysis, the samples were polished with silicon carbide (SIC) paper from P 800 to P 4000 and were then polished using diamond suspensions with powder sizes of 3 μm and 1 μm and Nap polishing cloths; then, active oxide polishing suspensions and Chem polishing cloths were used for polishing. The samples were observed through a back-scattered electron detector (BSED) image (SEM, Tamiang Layang, Indonesia)and energy-dispersive X-ray spectrometer (EDS) (Oxford Instruments, Abingdon, UK) mapping under the conditions of the voltage being 15.00 kV, the emission current being 213 μA, the chamber pressure being 4.29×10^{-6} mbar, and the gun pressure being 1.38×10^{-9} mbar.

The crystal structure and lattice constant of the alloy were derived by analyzing X-ray diffraction (XRD) patterns using Cu Kα radiation with the aid of an X-ray diffractometer (Empyrean, Malvern Panalytical, Almelo, The Netherlands). A Soller slit of 0.04°, a diversion slit of 1/8°, an anti-scattering slit of 1/4°, and a mask of 10 mm were used, and the φ spinning stage was used to increase the measuring area. To reduce the measuring time, a detector with 255 channels (PIXcel3D) was used, with XRD analysis of samples with a 2θ range from 30° to 90° measured with a step size of 0.026° and a time per step of 300°/s. To reduce the effect of texture, a wobbled scan with a step size of 5° and a range of 10° was used. XRD patterns were analyzed using the software HighScore from Malvern Panalytical.

A pin-on-disk sliding friction test of the alloy was performed by a multifunctional wear tester (RB102-PD, R&B, Daejeon, Republic of Korea) under dry sliding conditions at room temperature. The specimens were in the form of a cylindrical pin with a diameter of 4 mm and a height of 20 mm. A vertical pressure of 50 N was applied using a disk made of SKD11 steel. The rotating speed of the specimen was 764 RPM, and the rotating diameter was 28 mm. The test time for each specimen was set to approximately 20 min, and the total sliding length was approximately 13,441 m. Five tests were carried out for each alloy to confirm the wear loss results. The amount of wear was measured based on the weight of the sample before and after the test. Since hardness is one of the factors that indirectly measures a material's ability to resist wear, hardness testing was also conducted. A Vickers hardness tester was used, and five tests were conducted on each alloy specimen; from this, the average value was used. Using a load of 1 kgf, we conducted an indentation test using the Vickers Micro Hardness Tester (Aoli Shenzhen Technology Limited, Shenzhen, China), Mitutoyo Corporation's HM-220 (Mitutoyo, Aurora, IL, USA). The time was set to standard.

A compression experiment was performed at room temperature to investigate deformation behavior using a universal testing machine (5982B10532, INSTRON, Kaohsiung City, China). The size of the sample specimen was measured using a cylindrical specimen with a diameter of 4 mm and a height of 6 mm. The compression speed of the experiment was 0.06 mm/s, which is 1/100 of the specimen length, and the stopping condition was a

reduction of 50% of the load rate applied to the specimen. The experiment was conducted a total of three times.

3. Results and Discussion

3.1. XRD Phase Analysis

XRD analysis was performed to identify the phases in each sample. As shown in Figure 1, Stellite 6 consisted of a solid solution phase with a face-centered cubic (FCC) crystal structure, an M_7C_3 phase, and an M_2C phase, as reported previously [8]. The respective phase fractions were confirmed to be 58.5%, 38.2%, and 3.3%. The phase fractions were calculated by Rietveld refinement with FCC, M_7C_3, and M_2C phases. They usually occur after M_2C formation or after cementite formation if there has not been any intermediate M2X precipitation [9]. As a result of the XRD analysis, the M_7C_3 phase was determined to have an orthorhombic structure, and the space group was determined to be Pnma. The lattice parameters were a = 4.5 Å, b = 7 Å, and c = 12.1 Å. Carbon atoms existed in two different Wyckoff positions: C1 (8d) and C2 (4c). Metal atoms existed in five different Wyckoff positions: Cr1 (8d), Cr2 (4c), Cr3 (4c), Cr4 (4c), and Cr5 (8d). This result was based on the confirmation of the reference code ICSD 87129 in the XRD HighScore. The space group of the M_2C carbide was P63/mmc, and the lattice parameters were a = 3 Å, b = 3 Å, and c = 4.7 Å [10]. This result is based on the ICSD 167899 reference code. In the results of ICSD 5380, the lattice parameters for FCC were a = 3.6 Å, b = 3.6 Å, and c = 3.6 Å. It was confirmed that when the iron content in Stellite 6 increased to 20 wt%, the fractions of M_7C_3 and M_2C decreased to 31% and 0.5%, respectively. When the composition of Fe increased to 40 wt%, the XRD peak of the carbide disappeared. When the Fe weight ratio became 60 wt%, the XRD peak of the BCC phase appeared. According to the atomic radius table, the atomic radius of Fe is 140 pm, which is larger than the atomic radius of Co (135 pm); thus, as the content of Fe increases, the lattice parameter should increase [11]. The XRD experiment results revealed that the lattice parameters of the FCC phase in Stellite 6, Sample A, Sample B, and Sample C were 3.565 Å, 3.589 Å, 3.592 Å, and 3.598 Å, respectively. It can be observed that as the Fe concentration increased, the FCC lattice parameter progressively increased. The crystal structure of BCC was cubic, and the lattice parameters were a = 2.9 Å, b = 2.9 Å, and c = 2.9 Å. This information is based on reference code ICSD 180971. As shown in the XRD results, as the iron content increased and the carbide fraction decreased, the effect of precipitation hardening was lost, so elongation was expected to increase, and yield stress was expected to decrease.
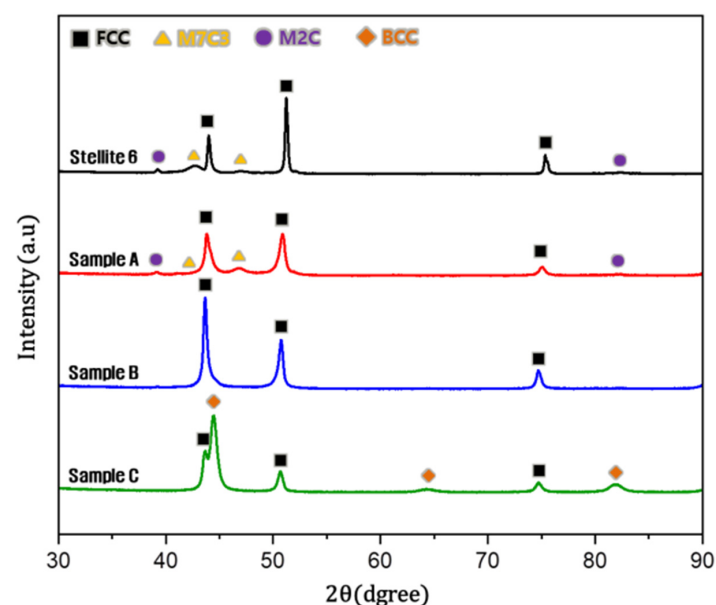

Figure 1. XRD phase analysis results of Stellite 6 according to the amount of Fe added.

3.2. BESD and EDS Observation

After XRD analysis, BSED analysis was performed to observe the microstructure. As shown in Figure 2, Stellite 6 was composed of three phases, consistent with the XRD analysis results. According to the XRD results, in Stellite 6, the FCC phase accounted for the largest fraction, followed by carbides. Carbides mainly existed as M_7C_3, while the others existed as M_2C. Therefore, the area of medium brightness, which occupied most of the area in the BSED image, was confirmed to be the FCC phase. To conduct an accurate analysis of carbides, EDS mapping was performed. According to the EDS mapping results shown in Figure 3, the darkest part of the BSED image was confirmed to be carbide composed of Cr and C, and the brightest part of the BSED image was confirmed to be carbide mainly composed of W [4,12–16].
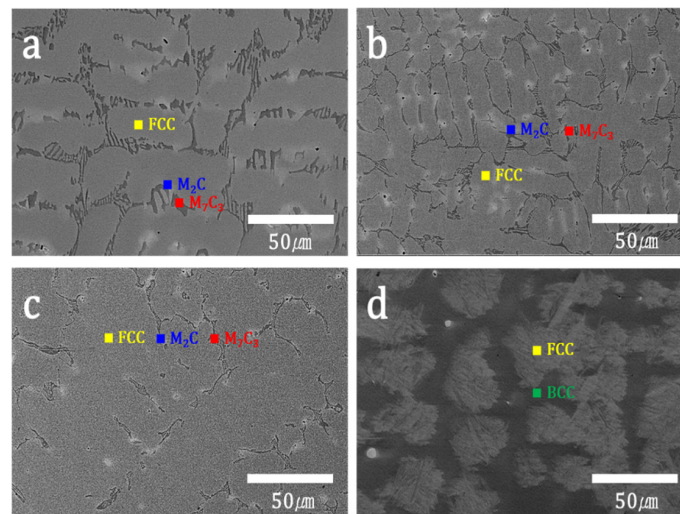

Figure 2. BSED image of Stellite according to the amount of Fe added: (**a**) Stellite 6 image, (**b**) Sample A image, (**c**) Sample B image, (**d**) and Sample C image.
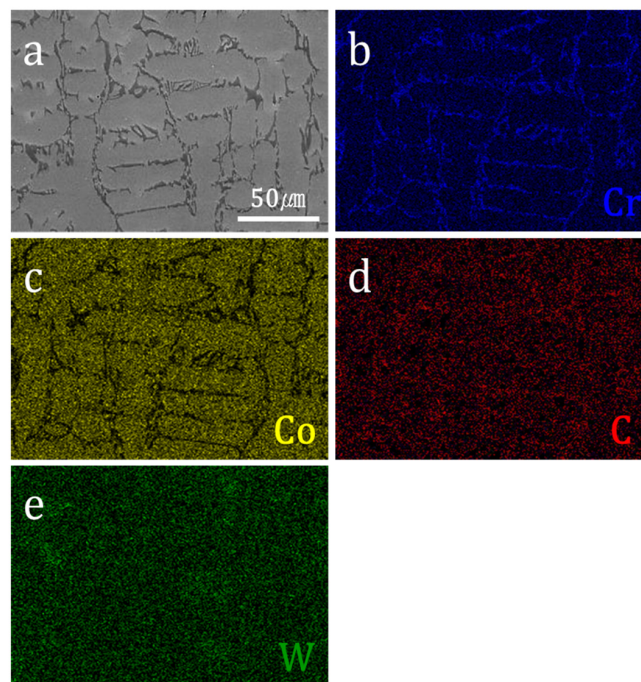

Figure 3. EDS mapping image of Stellite 6: (**a**) SEM image, (**b**) Cr mapping result, (**c**) Co mapping result, (**d**) C mapping result, (**e**) and W mapping result.

As shown in the results of the BSED analysis, the amount of carbide gradually decreased as the Fe content in the Stellite 6 raw material increased. In Sample C, the carbide phase disappeared, and a new phase was formed. From the XRD results, it can be seen that the body-centered cubic (BCC) phase appeared when the Fe content reached 60%. In general, if the difference in the constituent element ratio is not large, the FCC phase has a higher density than the BCC phase, so, in theory, it should appear brighter in the BSED image. According to the EDS mapping results of Sample C shown in Figure 4, the difference in components of the two phases was confirmed to be minimal, and the bright part due to the density difference can be seen to be the FCC phase [17].
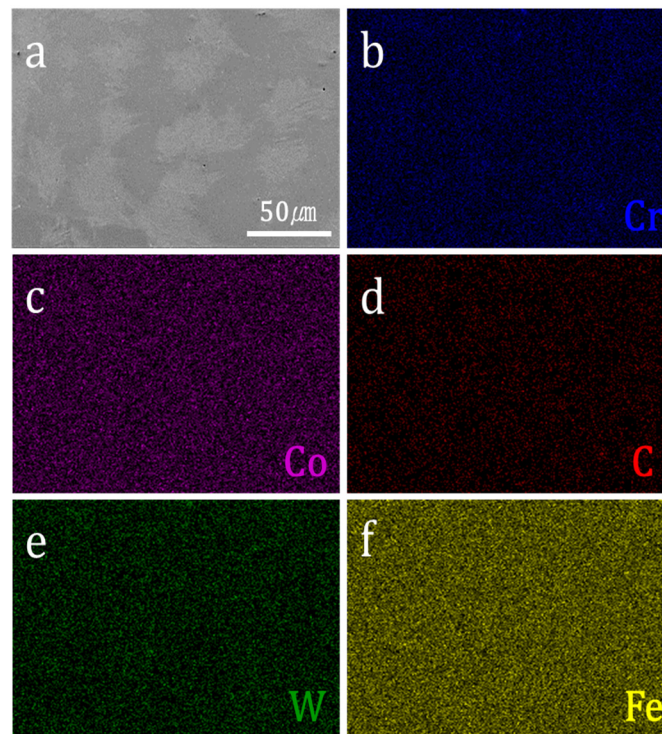

Figure 4. EDS mapping image of sample C. (**a**) Sem image, (**b**) Cr mapping result, (**c**) Co mapping result, (**d**) C mapping result, (**e**) W mapping result, and (**f**) Fe mapping result.

3.3. Abrasion Test

Abrasion testing is an experiment that shows the resistance of a material in the process of repeated friction with other materials. This test indicates the durability of a material for hard-facing. In general, the amount of carbide content in Stellite 6 has an effect on its wear resistance and hardness [17–20]. The average wear volume for each sample, derived from five wear tests, is shown in Figure 5a. As shown in Figure 5, Stellite 6, which had the highest carbide content, had the highest wear resistance, and Sample C, which did not contain carbides, had the lowest wear resistance. There was a relationship between wear resistance and hardness, and hardness was measured to confirm this. Stellite 6 contained three phases, the FCC phase, the M_7C_3 phase, and the M_2C phase, and each phase had different hardness characteristics [21,22]. The indenter tip was in the form of a conical diamond, with a vertex angle of 120° and a tip radius of 0.2 mm. Therefore, the results indicated the average hardness of the sample because the tip was larger than carbides, so the area touched by the indenter was included along with the carbide phase dispersed in the solid solution. Since the hardness of carbides was higher than that of matrix solid solutions, hardness was determined by the volume fraction of the carbide phases. As a result, it was confirmed that the Stellite 6 sample, in which carbides were distributed the

most, had the highest hardness value [22–28]. Additionally, the relationship between wear resistance and hardness can be confirmed by the equation below:
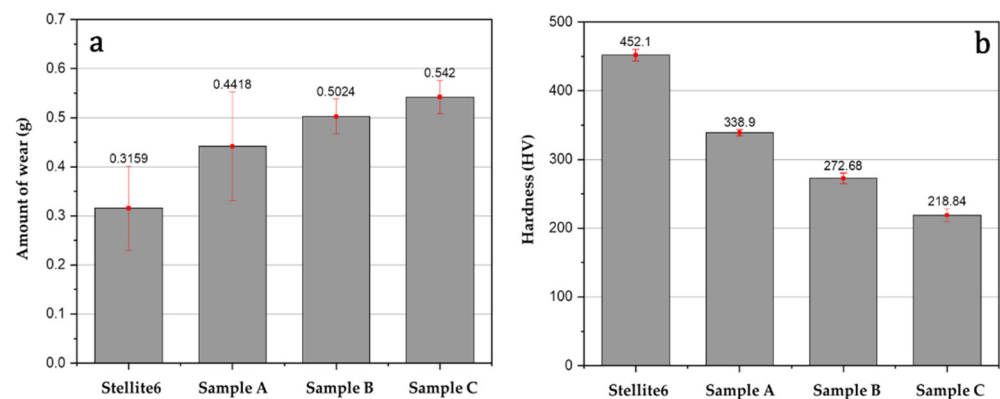
$$Q = \frac{KWL}{H}$$

Figure 5. (**a**) Graph of changes in wear amount according to Fe content and (**b**) changes in hardness value according to Fe content.

The above formulation references Archard's law in the study of friction and wear phenomena. The equation defines wear volume (Q) in relation to the material-specific wear coefficient (K), applied load (W), sliding distance (L), and material hardness (H). It can be seen that the wear volume Q of the specimen is inversely proportional to the hardness (H). However, the experimental calculation results did not match well. It is believed that this affects the wear resistance in addition to the hardness value. When using Archard's law to calculate the proportional constant, the K-values for each sample, the obtained values aligned with Table 3. These results signified extremely small and negligible values. A lower K-value within a proportional relationship indicates a relatively weak association between hardness (H) and wear volume (Q). Essentially, it implies that hardness does not directly influence wear. Other factors, apart from hardness, like applied load and sliding distance, may have a more significant impact on the relationship between hardness and wear. These findings allowed us to verify that hardness was not the only factor influencing the wear experiment results.

Table 3. Coefficients calculated using real experimental measurements and Archard's law.

Sample Name	Element and Content (wt%)				
	Q (g)	W (N)	L (m)	H (HV)	K $\left(\frac{\text{g·HV}}{\text{N·m}}\right)$
Stellite 6	0.3159 ± 0.086	50	13,441	451.2 ± 8.32	6.71×10^{-5}
Sample A	0.4418 ± 0.111	50	13,441	338.9 ± 4.42	5.88×10^{-5}
Sample B	0.5024 ± 0.0359	50	13,441	272.68 ± 7.66	9.39×10^{-5}
Sample C	0.542 ± 0.0335	50	13,441	218.84 ± 9.57	8.03×10^{-5}

3.4. Compression Test

Compression tests were performed on each sample to determine its potential for use as a hard-facing layer or buffering layer. Figure 6 shows the results of the compression experiment. Figure 7 is a graph that represents the yield stress. This means that plastic deformation occurred at the strain. According to the results of the compression tests, as shown in Figure 7, as the amount of Fe added increased, the yield stress decreased. It can be observed that the initial portions of specimens B and C closely resembled each other. As anticipated, the reduction in the quantity of carbides led to the elimination of precipitation hardening effects, resulting in a decrease in hardness values [29]. We were able to understand how the addition of Fe to Stellite 6 changed the material's strength and

deformation characteristics according to the results of the compression tests. This assisted in determining any material faults and gave information about the structural stability of each sample.
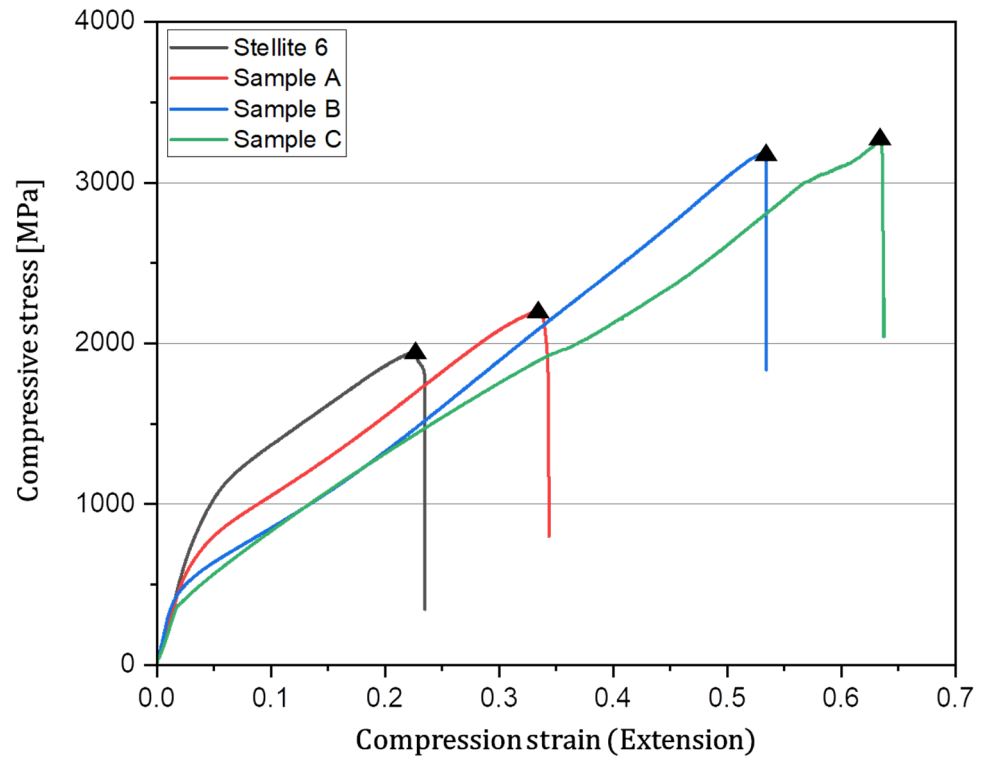

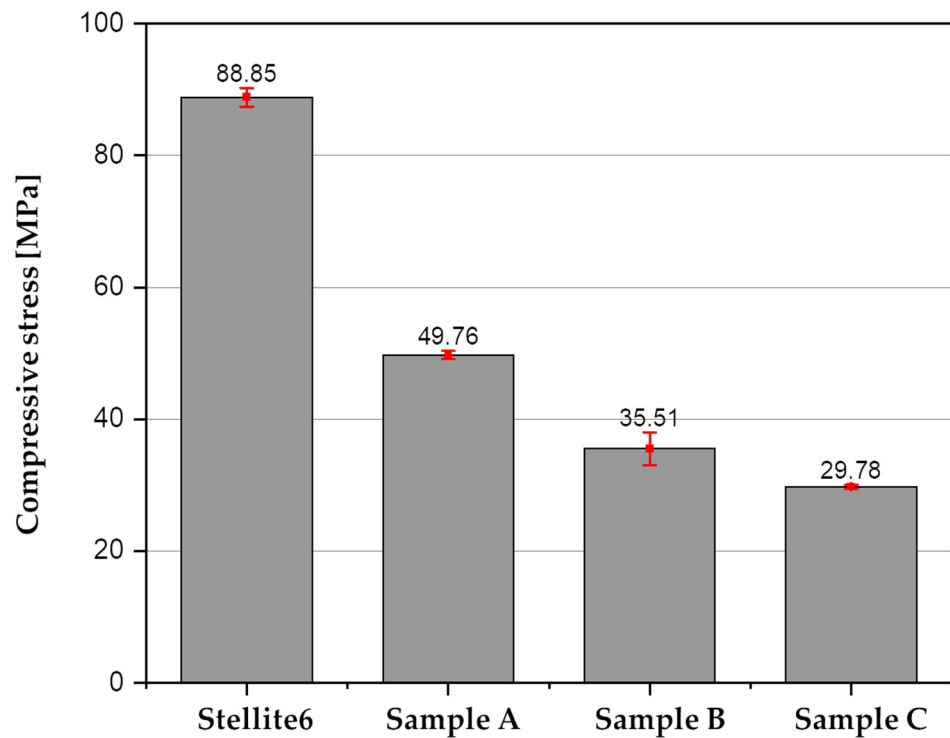**Figure 6.** Graph depicting the stress–strain curves from the compression tests.

Figure 7. Yield strength changes according to the compression experiment.

3.5. Coefficient of Thermal Expansion

TMA was performed to determine whether the thermal expansion coefficient of the sample was suitable as a buffer layer material. The way a material expands or contracts in response to temperature variations is represented by its coefficient of thermal expansion. It is a measurement of the thermal expansion qualities of a material and is frequently used to explain variations in physical attributes, such as area, volume, or length. This coefficient makes it easier to comprehend how an object's structure is impacted by thermal expansion or contraction. For example, it aids in understanding how partial deformations in an object occur due to thermal expansion or predicts changes in length due to temperature variations in materials. Figure 8 is the result of deriving the coefficient of thermal expansion (CTE). Each CTE at 300 °C is presented in the Figure 8. The method for calculating the value of the CTE is as follows [30,31].

$$\alpha = \frac{1}{L}\frac{\Delta L}{\Delta T}$$

where L is the length of the sample, ΔL is the amount of change in the length of the sample, and ΔT is the temperature change. The sample with the highest CTE value was Stellite 6, which means that it expands significantly when heat is applied. According to the above results, it was confirmed that the yield strength increased, and the hardness decreased as the amount of Fe added increased. The basic material used in this experiment, Fe, had a coefficient of thermal expansion (CTE) of 12.8 μm/m·°C, which is closest to that of carbon steel [32]. We calculated the thermal expansion coefficient using the previously given equation. As shown in Figure 8, the CTE values of Stellite 6 and Sample A were 15.87 μm/m·°C and 15.316 μm/m·°C. They cannot be used as a buffer layer due to the large difference compared to the CTE of carbon steel. Sample C was too low at 12.76 μm/m·°C, making it difficult to use as a buffer layer. The buffer layer in hard-facing mainly acts as wear and corrosion protection. It is therefore essential to choose an appropriate material for this purpose. It should possess hardness and thermal expansion coefficients equivalent to the base material. The chosen buffer layer preserves stability in relation to the foundation material. Therefore, Sample B, with an intermediate value, was considered suitable as a material for the buffer layer.
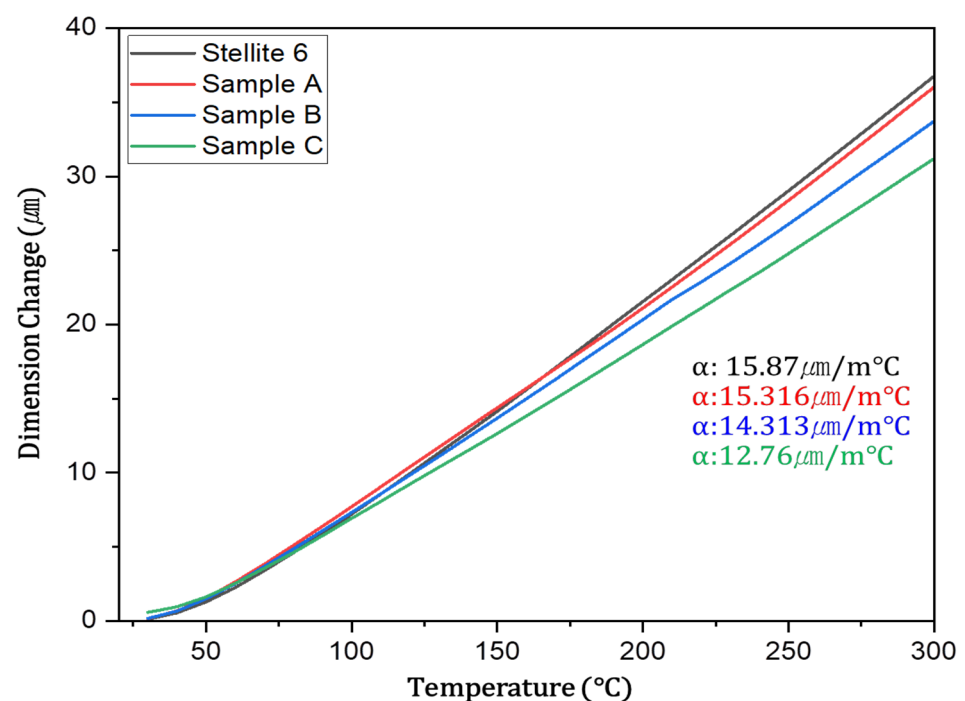

Figure 8. Results of the thermal mechanical analysis (TMA) for measuring and calculating the coefficient of thermal expansion (CTE).

4. Summary and Conclusions

In order to ascertain the ideal Fe concentration for the buffer layer in hard-facing procedures, this study examined Stellite 6 with additional Fe. Several phases were found during the XRD experiment carried out in this study, including the FCC, M_7C_3, M_2C, and BCC phases. Phase presence was influenced by changes in Fe composition, most notably by the introduction of a BCC phase at 60 wt% Fe and the elimination of carbides at 40 wt%, and 20 wt% Fe.

Three phases were validated by BSED and EDS observations, which showed that Stellite 6's carbides decreased as its Fe level increased. The absence of carbide in Sample C suggested the emergence of a new phase. Tests on wear and hardness revealed a relationship between carbide content and hardness/wear resistance. Nevertheless, there was a discrepancy between the experimental and computational results, indicating that wear resistance is influenced by more than just hardness.

Because there were fewer carbides in Sample C, the yield stress was lower, and the precipitate hardening removal increased the alloy ductility. Experiments using the coefficient of thermal expansion (CTE) showed that different samples had different CTE values. Sample A was unfit for the buffer layer, due to its excessive CTE. It was also not ideal that Sample C had a relatively low CTE. Sample B showed an intermediate CTE, indicating that it could be a suitable material for a buffer layer that sits between Sample C and Stellite 6's extremes. The material that successfully joined the base material and the cured layer was identified in this study as having an interim CTE.

The study's findings verify that a buffer layer in Stellite hard-facing can contain roughly 40% of the base material. We also came to the conclusion that leftover scrap from Stellite hard-facing that contains less than 40% Fe can be recycled and utilized again as a buffer layer. These findings are expected to have a major influence on future resource-recycling activities and offer important insights into scrap recycling in hard-facing operations.

Author Contributions: G.B.K., G.C.S. and S.C.H.: Investigation: performed the experiments, data curation, formal analysis; Y.D.K.: supervision, writing—review and editing; T.-W.N.: project administration, supervision, writing—review and editing, writing—review and editing; M.A.B.: Investigation: performed the experiments, data curation, formal analysis, writing—original draft preparation. All authors have read and agreed to the published version of the manuscript.

Data Availability Statement: The original contributions presented in the study are included in the article, further inquiries can be directed to the corresponding authors.

Conflicts of Interest: The authors declare no conflict of interest.

References

1. Singh, R.; Kumar, D.; Mishra, S.; Tiwari, S. Laser cladding of Stellite 6 on stainless steel to enhance solid particle erosion and cavitation resistance. *Surf. Coat. Technol.* **2014**, *251*, 87–97. [CrossRef]
2. Yao, M.; Wu, J.; Xie, Y. Wear, corrosion and cracking resistance of some W- or Mo-containing Stellite hardfacing alloys. *Mater. Sci. Eng. A* **2005**, *407*, 234–244. [CrossRef]
3. Thawari, N.; Gullipalli, C.; Katiyar, J.K.; Gupta, T. Influence of buffer layer on surface and tribomechanical properties of laser cladded Stellite 6. *Mater. Sci. Eng. B* **2021**, *263*, 114799. [CrossRef]
4. Shin, J.-C.; Doh, J.-M.; Yoon, J.-K.; Lee, D.-Y.; Kim, J.-S. Effect of molybdenum on the microstructure and wear resistance of cobalt-base Stellite hardfacing alloys. *Surf. Coat. Technol.* **2003**, *166*, 117–126. [CrossRef]
5. Venkatesh, B. Mechanical Behavior of Single and Multilayer Hardfacing on Ferrous Alloys. *Tribol. Charact. Surf. Coat.* **2022**, 281–305. [CrossRef]
6. Lolla, T.; Siefert, J.; Babu, S.S.; Gandy, D. Delamination failures of Stellite hardfacing in power plants: a microstructural characterisation study. *Sci. Technol. Weld. Join.* **2014**, *19*, 476–486. [CrossRef]
7. Thawari, N.; Gullipalli, C.; Katiyar, J.K.; Gupta, T. Effect of multi-layer laser cladding of Stellite 6 and Inconel 718 materials on clad geometry, microstructure evolution and mechanical properties. *Mater. Today Commun.* **2021**, *28*, 102604. [CrossRef]

8. Yao, Z.; Chen, Z.; Ouyang, M.; Chen, X.; Yang, M.; Li, Z.; Wang, C.; Yang, T.; Shi, R.; Zhong, Z.; et al. Accelerated discovery of composition-carbide-hardness linkage of Stellite alloys assisted by image recognition. *Scr. Mater.* **2023**, *234*, 115539. [CrossRef]

9. Li, X.; Xiong, J.; Zhang, L.; Yuan, X.; Zhao, P.; Yang, J.; Jiao, Y.; Zhang, H.; Chen, Z.; Li, T.; et al. Atom-scale characterization and 2D/3D modeling of carbides and FeCo phases in Stellite 6 laser clad coating after aging treatment. *Mater. Charact.* **2023**, *196*, 112645. [CrossRef]

10. Wu, X.; Chen, G. Microstructural features of an iron-based laser coating. *J. Mater. Sci.* **1999**, *34*, 3355–3361. [CrossRef]

11. Slater, J.C. Atomic Shielding Constants. *Phys. Rev. B* **1930**, *36*, 57–64. [CrossRef]

12. Kuzucu, V.; Ceylan, M.; Çelik, H.; Aksoy, I. Microstructure and phase analyses of Stellite 6 plus 6 wt.% Mo alloy. *J. Am. Acad. Dermatol.* **1997**, *69*, 257–263. [CrossRef]

13. Kong, G.; Zhang, D.; Brown, P.D.; McCartney, D.G.; Harris, S.J. Microstructural characterisation of high velocity oxyfuel thermally sprayed Stellite 6. *Mater. Sci. Technol.* **2003**, *19*, 1003–1011. [CrossRef]

14. Gorunov, A. Investigation of M7C3, M23C6 and M3C carbides synthesized on austenitic stainless steel and carbon fibers using laser metal deposition. *Surf. Coat. Technol.* **2020**, *401*, 126294. [CrossRef]

15. Gholipour, A.; Shamanian, M.; Ashrafizadeh, F. Microstructure and wear behavior of stellite 6 cladding on 17-4 PH stainless steel. *J. Alloys Compd.* **2011**, *509*, 4905–4909. [CrossRef]

16. Kishore, K.; Jaiswal, N.; Prabhakaran, A.; Arora, K.S. Through-thickness microstructure and wear resistance of plasma transferred arc Stellite 6 cladding: Effect of substrate. *CIRP J. Manuf. Sci. Technol.* **2023**, *42*, 24–35. [CrossRef]

17. Rabinowicz, E.; Tanner, R.I. Friction and wear of materials. *J. Appl. Mech.* **1966**, *33*, 479. [CrossRef]

18. Mutton, P.; Watson, J. Some effects of microstructure on the abrasion resistance of metals. *Wear* **1978**, *48*, 385–398. [CrossRef]

19. Xu, L.; Kennon, N.F. A study of the abrasive wear of carbon steels. *Wear* **1991**, *148*, 101–112. [CrossRef]

20. Khoddamzadeh, A.; Liu, R.; Liang, M.; Yang, Q. Wear resistant carbon fiber reinforced Stellite alloy composites. *Mater. Des.* **2014**, *56*, 487–494. [CrossRef]

21. Liu, R.; Wu, X.J.; Kapoor, S.; Yao, M.X.; Collier, R. Effects of Temperature on the Hardness and Wear Resistance of High-Tungsten Stellite Alloys. *Met. Mater. Trans. A* **2014**, *46*, 587–599. [CrossRef]

22. Vite, M.; Castillo, M.; Hernández, L.; Villa, G.; Cruz, I.; Stéphane, D. Dry and wet abrasive resistance of Inconel 600 and stellite. *Wear* **2005**, *258*, 70–76. [CrossRef]

23. Da Silva, W.S.; Souza, R.M.D.; Mello, J.D.B.; Goldenstein, H. Room temperature mechanical properties and tribology of NICRALC and Stellite casting alloys. *Wear* **2011**, *271*, 1819–1827. [CrossRef]

24. Huang, H.; Yi, G.; Wan, S.; Shan, Y.; Wang, W.; Deng, G. Influence of Al and Mo on microstructure and tribological behaviors of Co-based superalloy. *Mater. Chem. Phys.* **2023**, *308*, 128241. [CrossRef]

25. Quintero-Ortiz, J.; Guerra, F.; Bedolla-Jacuinde, A.; Leon-Patiño, C.A.; Pacheco-Cedeño, J.S. Sliding wear behavior of Co-Cr-Mo alloys with C and B additions for wear applications. *Wear* **2023**, *522*, 204698. [CrossRef]

26. Magarò, P.; Furgiuele, F.; Maletta, C.; Tului, M.; Wood, R.J.K. Wear Mechanisms of Cold-Sprayed Stellite-6 During Reciprocated Dry Sliding Under Different Sliding Speeds. *J. Therm. Spray Technol.* **2023**, *32*, 2336–2350. [CrossRef]

27. Kiehl, M.; Scheid, A.; Graf, K.; Ernst, B.; Tetzlaff, U. Coaxial laser cladding of cobalt-base alloy StelliteTM 6 on gray cast iron/investigations on friction, wear versus commercial brake pad, and corrosion characteristics. *Proc. Inst. Mech. Eng. Part D J. Automob. Eng.* **2023**, 09544070221145512. [CrossRef]

28. Han, W.; Cui, G.; Cui, H.; Kou, Z.; Liu, Y. Effect of Molybdenum on the Microstructure and High-Temperature Tribological Properties of Laser Clad CoCrW Coating. *Trans. Indian Inst. Met.* **2022**, *75*, 3193–3202. [CrossRef]

29. Ferozhkhan, M.M.; Duraiselvam, M.; Kumar, K.G.; Ravibharath, R. Plasma Transferred Arc Welding of Stellite 6 Alloy on Stainless Steel for Wear Resistance. *Procedia Technol.* **2016**, *25*, 1305–1311. [CrossRef]

30. Rajeev, G.; Rahul, M.; Kamaraj, M.; Bakshi, S.R. Microstructure and high temperature mechanical properties of wire arc additively deposited Stellite 6 alloy. *Materialia* **2020**, *12*, 100724. [CrossRef]

31. Yawei, Z.; Shixiao, Z.; Xudong, L. Thermal deformation behavior of Stellite 6B alloy. In *IOP Conference Series: Materials Science and Engineering*; IOP Publishing: Bristol, UK, 2021; p. 012012.

32. Wang, X.-L.; Hoffmann, C.M.; Hsueh, C.H.; Sarma, G.; Hubbard, C.R.; Keiser, J.R. Influence of residual stress on thermal expansion behavior. *Appl. Phys. Lett.* **1999**, *75*, 3294–3296. [CrossRef]